Joule-Thomson Cooling During CO2 Injection Under Unsteady-State Delayed Heat Exchange

Chesnokov, Christina; Prempeh, Kofi Ohemeng Kyei; Farajzadeh, Rouhi; Bedrikovetsky, Pavel

DOI
10.1029/2024WR038466

Publication date
2025

Document Version
Final published version

Published in
Water Resources Research

Citation (APA)
Chesnokov, C., Prempeh, K. O. K., Farajzadeh, R., & Bedrikovetsky, P. (2025). Joule-Thomson Cooling During CO2 Injection Under Unsteady-State Delayed Heat Exchange. *Water Resources Research*, *61*(6), Article e2024WR038466. https://doi.org/10.1029/2024WR038466

Water Resources Research®

RESEARCH ARTICLE
10.1029/2024WR038466

Joule-Thomson Cooling During CO_2 Injection Under Unsteady-State Delayed Heat Exchange

Christina Chesnokov[1], **Kofi Ohemeng Kyei Prempeh**[1], **Rouhi Farajzadeh**[2,3], and **Pavel Bedrikovetsky**[1]

[1]School of Chemical Engineering, The University of Adelaide, Adelaide, SA, Australia, [2]Shell Global Solutions International, The Hague, The Netherlands, [3]Faculty of Civil Engineering and Geosciences, Delft University of Technology, Delft, The Netherlands

Key Points:

- 1D non-isothermal flow problem, where heat exchange starts at the moment of gas front arrival, allows for an exact solution
- This analytical model for 1D flow allows calculating maximum injection rate of CO_2 preventing hydrate formation
- Exact-solution-based validation technique of transversal heat-exchange model with surrounding layers for any 1D transport

Correspondence to:
P. Bedrikovetsky,
pavel.bedrikovetski@adelaide.edu.au

Citation:
Chesnokov, C., Prempeh, K. O. K., Farajzadeh, R., & Bedrikovetsky, P. (2025). Joule-Thomson cooling during CO_2 injection under unsteady-state delayed heat exchange. *Water Resources Research*, *61*, e2024WR038466. https://doi.org/10.1029/2024WR038466

Received 19 JUL 2024
Accepted 13 MAY 2025

Abstract

Joule-Thomson cooling during CO_2 injection into low-pressure fields can lead to injectivity impairment due to hydrate formation. This paper presents axial-symmetric flow model, which can be used to predict propagation of temperature and CO_2 fronts during CO_2 injection into porous formations accounting for Joule-Thomson cooling and unsteady-state delayed heat exchange between the reservoir and the adjacent formations. The solution of the 1D flow is validated by comparing with the quasi 2D analytical heat-conductivity solution. The non-steady state heat exchange results in a temperature front that propagates without limit into the reservoir with time. The temperature profiles exhibit a temperature decrease from the injected temperature to a minimum value, followed by a sharp increase to initial reservoir temperature on the temperature front. The solution allows plotting temperature-pressure (*T-P*) profiles at fixed moments in the CO_2-water phase diagram. By changing injection parameters such as injection rate, the *T-P* trajectories allow for assessment of hydrate formation.

Plain Language Summary

Joule-Thomson cooling and heat exchange with surrounding formations can highly affect CO_2 injection into aquifers and depleted gas fields. These effects can lead to rock drying, salt precipitation, and fines migration. To prevent and mitigate these injectivity damage processes, fast and accurate prediction of the reservoir temperature field is required. This study develops one-dimensional heat transfer equation that captures the above-mentioned mechanisms and derives exact solution for radial CO_2 injection. A novel validation procedure of the model self-consistency without the need for two-dimensional numerical model has been proposed. It was found that the largest temperature drop occurs from well to the temperature front, with minimal changes ahead of the front. The exact solution allows calculating the maximum injection rate to avoid hydrate formation.

1. Introduction

The reduction of greenhouse gas emissions, particularly Carbon Dioxide (CO_2), is pivotal to controlling global climate change (Raimi et al., 2024). One approach involves capturing CO_2 from concentrated sources like industrial plants or directly from the atmosphere, and storing it underground, for example, in depleted oil and gas reservoirs and aquifers (Barrufet et al., 2010; Michael et al., 2010). Prior knowledge of reservoir properties provides advantages due to the demonstrated capacity for fluid containment (Barrufet et al., 2010). However, the characteristic low pore pressures in these reservoirs post-depletion can induce considerable Joule–Thomson (JT) cooling upon CO_2 injection, due to substantial pressure differentials (Mathias et al., 2010). The JT cooling phenomenon refers to the decrease in temperature experienced by a real gas, like CO_2, as it expands from high to low pressure under adiabatic conditions (Maloney & Briceno, 2009). Some extra cooling is due to water evaporation into injected CO_2. This cooling effect may lead to operational challenges such as freezing of pore fluids or formation of CO_2 or Methane (CH_4) hydrates, impairing the injectivity of wells (Aghajanloo et al., 2024; Oldenburg, 2007). Addressing these concerns requires the utilization of mathematical tools to identify operational constraints susceptible to the JT cooling effect, and to devise effective mitigation strategies.

Mathias et al. (2010) derived an exact solution for CO_2 injection, considering JT cooling within an adiabatic reservoir, that is, without accounting for heat exchange with surrounding formations. The schematic for flow and heat fluxes is presented in Figure 1a, which exhibits the heat supply into cooled-down reservoir from the adjacent layers. The model provides explicit formulas for temperature and pressure profiles; identifies the cold front position; and evaluates the impact of permeability and initial pressure on the magnitude of JT effect. This

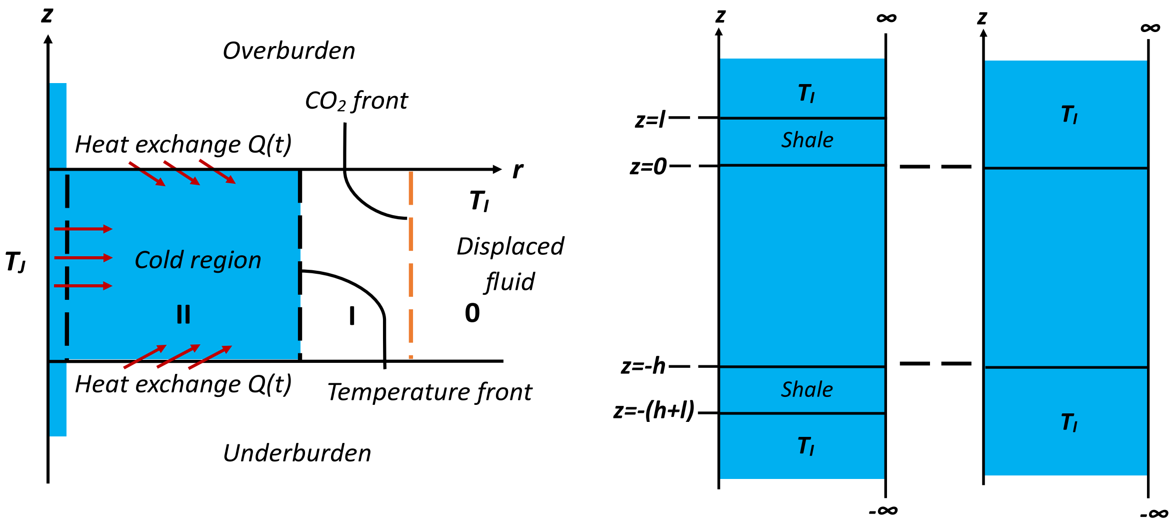

(a) (b) (c)

Figure 1. Schematic of CO2 injection into a depleted reservoir. (a) Reservoir cross section; (b) steady-state temperature distribution in shales above and below the reservoir; (c) transitional temperature wave in semi-infinite adjacent formations.

analytical model can serve as a benchmark for numerical methods for CO_2 injection including various storage scenarios (Moreno et al., 2021; Moreno & Rabinovich, 2021; Norouzi et al., 2022; Rabinovich et al., 2016).

However, heat exchange between the reservoir and adjacent layers significantly impacts non-isothermal flows in porous media (LaForce et al., 2014; Lawal, 2020). Chesnokov et al. (2024) derived an exact solution for CO_2 injection into a non-adiabatic reservoir accounting for JT cooling. The model represents a reservoir bounded by impermeable shales, followed by semi-infinite adjacent layers, as it is shown in Figure 1b. Within the shales, a steady-state temperature distribution is assumed, while initial temperature is maintained in the adjacent formations. Therefore, the model assumes the Newton's law for heat-exchange rate, which is proportional to the temperature difference between the reservoir and the adjacent layers. A comparison of the adiabatic and steady-state heat-exchange models shows a significant influence of heat exchange on the temperature profile. In particular, the heat supplied by the adjacent formations slows down the penetration depth and reduces the temperature drop between the well and the temperature front. The minimum temperature in the model with heat exchange can be significantly higher compared to the adiabatic case. The temperature profile stabilizes with time.

Figure 1c presents a more realistic geological setting of direct contact between the reservoir and the adjacent formations. The decreasing reservoir temperature propagates into the semi-infinite surrounding layers as a transient heat wave. An analytical model for CO_2 injection for this case is not available.

For two-phase non-isothermal flows, the exact solutions with steady-state heat exchange, like that in Figure 1b, are obtained by the splitting method (Borazjani & Bedrikovetsky, 2017; Pires et al., 2006). The exact solution for unsteady-state heat exchange without delay during two-phase flow follows from the expression of Riemann invariants (Bedrikovetsky, 1993).

The present work fills the gap and derives an analytical model for CO_2 injection, which accounts for a non-steady state heat exchange between the reservoir and semi-infinite adjacent formations. The derived explicit formula allows for the analysis of temporal evolution of temperature profiles. Unlike the steady state model, the unsteady-state model reveals no profile stabilization over time. The explicit formulas determines the temperature and pressure profiles at a fixed time, which calculates the path of radial dependency in CO_2-water phase diagram; the path connects the well and the reservoir. Hydrates do not form if the paths corresponding to all moments are located outside the hydrate-formation envelope; therefore, the analytical model allows calculating the maximum injection rate preventing hydrate formation. Validation of the model was conducted through comparison with the exact solution for 2D vertical heat conduction problem.

The structure of the paper is as follows. Section 2 describes the assumptions for the mathematical model and outlines the governing equations. Section 3 presents the exact solution of the model. Section 4 validates the analytical model by comparison with the 2D heat transfer problem. Section 5 gives the qualitative analysis of temperature profiles and their dynamics. Section 6 provides the risk assessment for hydrate formation and compares *T-P* profiles obtained by various heat-exchange models. Section 7 presents the sensitivity analysis. Section 8 concludes the paper.

2. Mathematical Model

This section presents the mathematical model for temperature profile evolution during CO_2 injection: the assumptions of the model (Section 2.1), the form of the unsteady-state heat-exchange rate term (Section 2.2), the governing equations (Section 2.3) and the dimensionless form of the model (Section 2.4).

2.1. Model Assumptions

The model assumptions are: (a) 1-D radial unsteady-state single-phase non-isothermal flow in an infinite homogeneous reservoir; (b) reservoir fluids—brine and CO_2—and rock are incompressible; (c) connate water saturation S_{wi} in the reservoir; (d) the temperature of the injected CO_2 at the injection point in the wellbore is constant; (e) Joule-Thomson (JT) coefficient, permeability, porosity, heat conductivity and heat capacity of rock and fluid are constant; (f) CO_2 is injected at a constant rate, and pressure at drainage radius (reservoir pressure) is constant; (g) water evaporation into gaseous phase is neglected; (h) density and viscosity of fluids are constant; and (i) the form of the heat exchange between the surrounding formations and the reservoir follows self-similar vertical heat transfer with delay due to the arrival of the CO_2 front; (j) no leakage of the reservoir fluid into the adjacent formations; (k) no hydrates are formed during the injection.

Assumptions (a)–(h) are common and have been widely used in mathematical modeling of non-isothermal flows in porous media (LaForce et al., 2014; Lawal, 2020). Regarding assumption (d), the well-head temperature is assumed constant. The column volume is negligible compared to the injected volume, meaning the flow within the column is considered to be steady-state. Therefore, JT effect in the column is also assumed to be steady-state. Both assumptions result in a constant CO_2 temperature at the wellbore.

Assumption (i) corresponds to the "vertical" heat exchange of the reservoir with semi-infinite overburden and under-burden formations Figure 1c. The form of non-equilibrium heat-exchange rate is supported by the derivations in Appendix A and Section 2.2. Appendix B formulates the governing equation using the non-equilibrium heat-exchange rate, Appendix C derives an exact solution and Appendix D presents the heat exchange term validity domain.

The fluid ahead of the CO_2 front could be either water (for CO_2 storage in aquifers) or gas and water (for CO_2 storage in depleted gas reservoirs). The temperature ahead of the CO_2 front remains equal to the initial reservoir temperature of $T = T_I$.

All coefficients in Equations B7–B9 are functions of temperature; in this model they are assumed to be constant. Therefore, Equation C2 is a linear partial differential equation (PDE) allowing for exact solution by method of characteristics (Polyanin & Zaitsev, 2003). Three temperature domains are defined by the two fronts: a temperature front and CO_2 front. These fronts divide the (x, t_D) plane into three zones- 0, I and II, as illustrated in Figure 2. In domain 0, ahead of the CO_2 front, the system is at its initial condition. Domain I is located in between the temperature and the CO_2 front. The characteristic lines propagating in this domain originate from the moving CO_2 front and are parallel to the temperature front. In the last domain, II, characteristics originate from injection well and propagate behind the temperature front.

2.2. The Unsteady-State Heat-Exchange Rate Term

Non-steady heat exchange occurs between the reservoir and the surrounding semi-infinite formations. Appendix A solves the classical 1D equation for the heat transfer over the vertical coordinate (Equation A1) with the boundary conditions given by Equations A3–A5. Calculation of the temperature gradient from the solution $T(z,t)$ at $z = 0$ yields the heat exchange term (Equation A7). The temperature at the interface given by T_J (K) is substituted by the unknown reservoir temperature $T(r,t)$ (K). The temperature ahead of the gas front is equal to the initial temperature T_I, so that heat exchange in point r starts at the moment of the arrival of the CO_2 front. We assume Equation A7 to be valid for the case where the reservoir temperature T_r is not constant and is equal to the current reservoir temperature $T(r,t)$, that is, constant T_r in Equation A7 is substituted by $T(r,t)$ in Equation 1.

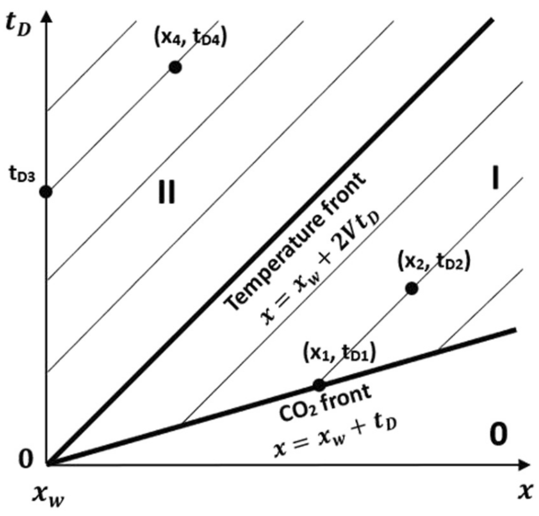

Figure 2. Characteristic lines in the (x, t_D) plane.

Consequently, delay in the front arrival defined by Equation A8, is introduced into heat exchange term in Equation A7, reformulating the heat exchange term as:

$$Q(r,t) = \gamma\left(\frac{\partial T}{\partial z}\right)_{z=0} = -\sqrt{\frac{\gamma\left[\phi\rho_w C_{p_w} + (1-\phi)\rho_s C_{p_s}\right]}{\pi}}\;\frac{T(r,t) - T_I}{\sqrt{t - \frac{\pi r^2 - \pi r_w^2}{u}}} \quad (1)$$

where Q (MT^{-3}) is the heat exchange, γ ($MLT^{-3}K^{-1}$) is the heat conductivity of the adjacent formations, φ is porosity, ρ_w (ML^{-3}) is the water density, C_{pw} ($L^2T^{-2}K^{-1}$) is the water specific heat capacity, ρ_s (ML^{-3}) is the solid density, C_{ps} ($L^2T^{-2}K^{-1}$) is the solid specific heat capacity, T(K) is temperature, T_I (K) is the initial reservoir temperature, r_w (L) is the well radius and u (L^2T^{-1}) is the effective injection rate per unit of the reservoir thickness. Here the units for all quantities are presented in the brackets, where M, T, L, and K correspond to mass, time, length, and temperature, respectively.

Further in the text, we call the term in Equation 1 the heat exchange rate of the reservoir with surrounding formations to close the governing energy-balance equation (Bedrikovetsky, 1993; Lake, 1989). The major assumption that supports Equation 1—proportionality between the current reservoir temperature *T(r,t)* and the initial temperature T_I—will be checked during the analytical model validation in Section 4.

The assumption of the initial reservoir temperature maintained ahead of the CO_2 front, causing the delay in Equation 1, is based on the incompressibility of the displaced fluid with no Joule-Thomson effect. During gas injection into a depleted or low-pressure reservoir, initially saturated with water and a compressible fluid such as gas, pressure gradient becomes negative from the start of injection; the temperature gradient also becomes non-zero. Therefore, the temperature difference between the reservoir and surrounded formations becomes non-zero from the moment $t = 0$, resulting in the heat exchange expression (Equation A7), that is, without any delay.

2.3. Governing Equations

The energy-balance equation consists of the heat capacity of the rock, CO_2, and water, advective heat transport, the JT effect, and heat exchange with the adjacent layers:

$$\left[(1-\phi)\rho_s C_{p_s} + \phi(1-S_{wi})\rho_g C_{p_g} + \phi S_{wi}\rho_w C_{p_w}\right] h\frac{\partial T}{\partial t} + \rho_g C_{p_g}\frac{q}{2\pi r}\frac{\partial}{\partial r}\left[T - \alpha_{JT}p\right] = -\sqrt{\frac{\gamma\left[\phi\rho_w C_{p_w} + (1-\phi)\rho_s C_{p_s}\right]}{\pi}}\;\frac{(T - T_I)}{\sqrt{t - \frac{\pi r^2 - \pi r_w^2}{u}}} \quad (2)$$

where S_{wi} is the initial water saturation (assumed to be immobile in this paper), ρ_g (ML^{-3}) is the gas density, C_{pg} ($L^2T^{-2}K^{-1}$) is the gas specific heat capacity, h(L) is the half-thickness of the reservoir, q(L^3T^{-1}) is half of the injection rate, α_{JT}($M^{-1}LT^2K$) is the JT coefficient and p($ML^{-1}T^{-2}$) is the fluid pressure. Appendix B provides the detailed derivation of the energy balance in Equation 2.

Further, the effective injection rate of CO_2, per unit of formation thickness, is defined as:

$$u = \frac{q}{(1-S_{wi})\phi h} \quad (3)$$

The pressure gradient in the reservoir is calculated using Darcy's law:

$$\frac{\partial p}{\partial r} = -\frac{\mu q}{2\pi r h K_{rgwi} k} \quad (4)$$

where μ ($\mathrm{ML}^{-1}\mathrm{T}^{-1}$) is viscosity of CO_2, K_{rgwi} is the end-point relative permeability of CO_2, rate q is constant, and $k(\mathrm{L}^2)$ is permeability.

The position of the gas front, $r_f(t)$, follows from Equation 3, and for $t = t_j$, the position of the gas front at the end of injection is r_e (L):

$$\pi r_f^2(t) = ut \Rightarrow \pi {r_e}^2 = ut_j \tag{5}$$

One pore volume injected (PVI) corresponds to the reservoir volume swept by the injected gas at $t = t_j$.

The boundary condition imposed at the wellbore corresponds to the injection of CO_2 at a constant temperature:

$$T(r = r_w) = T_J \tag{6}$$

where T_J (K) is the injected fluid temperature.

The model assumes that an incompressible fluid moves ahead of the CO_2 front, where there is no JT cooling effect in this zone. Therefore, the temperature remains constant at its initial value in this area. Heat exchange with the surrounding layers starts at the moment of the CO_2 front arrival, as it is shown in Appendix A. The boundary condition imposed on the gas front:

$$T\left(\sqrt{\frac{ut}{\pi} + {r_w}^2}, t\right) = T_I \tag{7}$$

2.4. Dimensionless System

The following dimensionless variables are introduced to obtain a dimensionless energy-balance equation:

$$T_D = \frac{T - T_I}{T_I - T_J};\ t_D = \frac{t}{t_j}; r_D = \frac{r}{r_e};\ r_{Dw} = \frac{r_w}{r_e} \tag{8}$$

The substitution of Equation 8 into Equation 2 results in the dimensionless form of energy balance:

$$\frac{\partial T_D}{\partial t_D} + \frac{V}{r_D}\frac{\partial T_D}{\partial r_D} = -\frac{A}{{r_D}^2} - B\frac{T_D}{\sqrt{t_D - \left({r_D}^2 - {r_{Dw}}^2\right)}} \tag{9}$$

here the dimensionless groups A, B, and V are:

$$A = \frac{\alpha_{JT} q \mu \rho_g C_{p_g}(1 - S_{wi})\phi}{\left[(1-\phi)\rho_s C_{p_s} + \phi(1 - S_{wi})\rho_g C_{p_g} + \phi S_{wi}\rho_w C_{p_w}\right] 4\pi k h K_{rgwi}(T_I - T_J)} \tag{10}$$

$$B = \sqrt{\frac{\gamma\left[\phi\rho_w C_{p_w} + (1-\phi)\rho_s C_{p_s}\right] t_j}{\pi h^2\left[(1-\phi)\rho_s C_{p_s} + \phi(1 - S_{wi})\rho_g C_{p_g} + \phi S_{wi}\rho_w C_{p_w}\right]^2}} \tag{11}$$

$$V = \frac{\rho_g C_{p_g}(1 - S_{wi})\phi}{2\left[(1-\phi)\rho_s C_{p_s} + \phi(1 - S_{wi})\rho_g C_{p_g} + \phi S_{wi}\rho_w C_{p_w}\right]} \tag{12}$$

The dimensionless constant A is called the JT number, dimensionless constant B—the heat exchange number and V—the dimensionless velocity of the temperature front.

Equation 2 assumes equal heat capacities and densities of the reservoir and surrounding formations rocks. If those are different, the properties of the reservoir rock enter in denominator of constant B, and the properties of the adjacent layers enter its nominator. The constants A and V remain the same.

Substituting dimensionless variables from Equation 8 into boundary conditions in Equations 6 and 7 gives the dimensionless form of boundary condition at the wellbore:

$$T_D(r_D = r_{Dw}, t_D) = -1 \tag{13}$$

and at the CO_2 front:

$$T_D\left(r_D = \sqrt{{r_{Dw}}^2 + t_D}\,, t_D\right) = 0 \tag{14}$$

3. Exact Analytical Solution

The exact solution of Equation 9 is derived in linear coordinates (x,t) in Appendix C. Energy balance Equation 9 is valid behind the water-gas front; temperature ahead is equal to T_I. The dimensionless speed of this front is equal to one. Equation 12 presents the temperature front speed V, which is smaller than one. This is explained by an equal temperature in gas, rock, and residual water. The temperature wave moves throughout the overall rock-fluid volume, while gas propagates only via the $\phi(1\text{-}S_{wi})$ fraction. Therefore, the temperature front lags behind the water-gas front (Figures 1 and 2). These two fronts separate the flow domain into three zones: 0, I, and II. In domain 0, ahead of the CO_2 front, the system remains at the initial conditions. Domain I is located in between the temperature and the CO_2 fronts. Figure 2 shows that the temperature $T(x,t)$ propagates into domain I from the water-gas front along characteristics with speed $2V$. It propagates into domain II along characteristics from the axes t where the boundary conditions are set.

The substitution of the linear variables given by Equation C1 into the overall temperature profile in Equation C15 yield the radial dimensionless form of the temperature profile:

$$T_D(r_D,t_D) = \begin{cases} e^{\frac{2B}{2V-1}\sqrt{t_D-({r_D}^2-{r_{Dw}}^2)}}\left(-e^{-\frac{2B}{2V-1}\sqrt{t_D-\frac{{r_D}^2-{r_{Dw}}^2}{2V}}} - \dfrac{A}{V}\displaystyle\int_{r_{Dw}}^{r_D}\frac{1}{k}e^{-\frac{2B}{2V-1}\sqrt{t_D-(k^2-{r_{Dw}}^2)}}\,dk\right), & t_D > \dfrac{{r_D}^2-{r_{Dw}}^2}{2V} \\ -\dfrac{A}{V}e^{\frac{2B}{2V-1}\sqrt{t_D-({r_D}^2-{r_{Dw}}^2)}}\displaystyle\int_{\sqrt{\frac{\left(t_D+{r_{Dw}}^2-\frac{{r_D}^2}{2V}\right)}{1-\frac{1}{2V}}}}^{r_D}\frac{1}{k}e^{-\frac{2B}{2V-1}\sqrt{t_D-(k^2-{r_{Dw}}^2)}}\,dk, & {r_D}^2-{r_{Dw}}^2 < t_D < \dfrac{{r_D}^2-{r_{Dw}}^2}{2V} \\ 0, & {r_D}^2-{r_{Dw}}^2 > t_D \end{cases} \tag{15}$$

The substitution of the variables given in Equation 8 into Equation 15 results in the dimensional form of the temperature profile:

$$T(r,t) = \begin{cases} T_I + (T_J - T_I)\,e^{-\frac{2bu}{u-2\pi w}\sqrt{t-\frac{\pi r^2-\pi {r_w}^2}{u}}}\left(e^{\frac{2bu}{u-2\pi w}\sqrt{t-\frac{r^2-{r_w}^2}{2w}}} - \dfrac{m}{w}\displaystyle\int_{r_w}^{r}\frac{1}{k}e^{\frac{2bu}{u-2\pi w}\sqrt{t-\frac{\pi k^2-\pi {r_w}^2}{u}}}\,dk\right), & t \geq \dfrac{r^2-{r_w}^2}{2w} \\ T_I - (T_J - T_I)\,\dfrac{m}{w}e^{-\frac{2bu}{u-2\pi w}\sqrt{t-\frac{\pi r^2-\pi {r_w}^2}{u}}}\displaystyle\int_{\sqrt{\frac{t+\frac{\pi}{u}{r_w}^2-\frac{r^2}{2w}}{\left(\frac{\pi}{u}-\frac{1}{2w}\right)}}}^{r}\frac{1}{k}e^{\frac{2bu}{u-2\pi w}\sqrt{t-\frac{\pi k^2-\pi {r_w}^2}{u}}}\,dk, & \dfrac{\pi r^2-\pi {r_w}^2}{u} \leq t < \dfrac{r^2-{r_w}^2}{2w} \\ T_I, & \dfrac{\pi r^2-\pi {r_w}^2}{u} > t \end{cases} \tag{16}$$

Table 1
Model Parameters Used in This Study

Parameter	Symbol	Base case	Minimum	Maximum	Unit
Half of reservoir thickness	h	91	1	100	m
Porosity	φ	0.11	0.1	0.3	[−]
Absolute permeability	k	2×10^{-15}	4×10^{-16}	6×10^{-14}	m^2
End point relative permeability	K_{rgwi}	1	1	1	[−]
Well radius	r_w	0.1	0.05	0.13	m
Rock density	ρ_s	2,600	2,270	3,200	kg/m^3
Water density	ρ_w	992	527	1,000	kg/m^3
CO_2 density	ρ_f	141.4	0.5	1,236	kg/m^3
CO_2 viscosity	μ_f	16.7×10^{-5}	1.1×10^{-5}	2.7×10^{-4}	Pa.s
Heat capacity of rock	c_S	1,000	776	1,215	J/kg/K
Heat capacity of water	c_w	4,037	3,965.1	4,335.4	J/kg/K
Heat capacity of CO_2	c_f	904	709	1,476	J/kg/K
Joule Thomson coefficient	α_{JT}	10.2×10^{-6}	7×10^{-6}	1.08×10^{-5}	K/Pa
Adjacent formation heat conductivity	γ	2.5	1	3.7	W/m/K
Well pressure	p_w	50×10^5	50×10^5	50×10^5	Pa
Reservoir temperature	T_I	378.15	294.15	398.15	K
Injection temperature	T_J	293.15	293.15	293.15	K
Injection time	t_j	10	0.00274	20	Years
Half of CO_2 injection flow rate	q	0.02	0.005	0.04	m^3/s
Connate water saturation	S_{wi}	0.2	0.2	0.4	[−]

Here the dimensional constants w (L^2T^{-1}), m (L^2T^{-1}) and b $(T^{-1/2})$ are:

$$w = V\frac{r_e{}^2}{t_j};\; m = A\frac{r_e{}^2}{t_j};\; b = \frac{B}{\sqrt{t_j}}; \tag{17}$$

4. Validation of the Analytical Model

The validation of the analytical model is achieved by comparing the solution obtained in Section 3 with the solution for the quasi 2D heat conductivity problem, derived in Appendix D. For a known reservoir temperature profile in Equation 15, we calculate heat exchange with the surrounding formations, given by Equation 1. Equation D4 defines the boundary condition for the 2D heat conductivity problem as the heat flux on the interface or boundary between the reservoir and the adjacent formations. The solution for the "vertical" heat exchange $T_D(z_D,t_D)$ is presented in Appendix D by Equation D10. Finally, Equation D11 gives the temperature profile at the interface by substituting $z_D = 0$ into Equation D10. The validation is achieved by comparison of Equation D11 to the dimensionless reservoir temperature profile in Equation 15, that is, by assuring the model self-consistency.

The parameter values for the base case used in all further calculations are presented in Table 1.

The analysis of the effect of the dimensionless groups A, B, and V, presented in Figure 4, is using the following variation intervals for these groups: A ranges from 3.93×10^{-10} to 4.78×10^3, representing the magnitude of the JT effect on the temperature profile, B ranges from 6.22×10^{-4} to 3.33×10^1, demonstrating the effect of NSS heat exchange, V ranges from 2.98×10^{-6} to 1.35×10^{-1}, indicating the delay of the temperature front as compared with the gas-water front. The temperature profile inside the reservoir is denoted as $T_{1D}(r_D,t_D)$ and the temperature profile along the interface for the vertical 2D problem is referred to as $T_{2D}(z_D = 0,t_D)$.

Figure 3 shows that an absolute error—deviation between $T_{1D}(r_D,t_D)$ and $T_{2D}(z_D = 0,t_D)$—reaches maximum at the temperature front and then decreases within a small distance from it. This stems from the step function behavior of the two plots, where the maximum error occurs around the discontinuity.

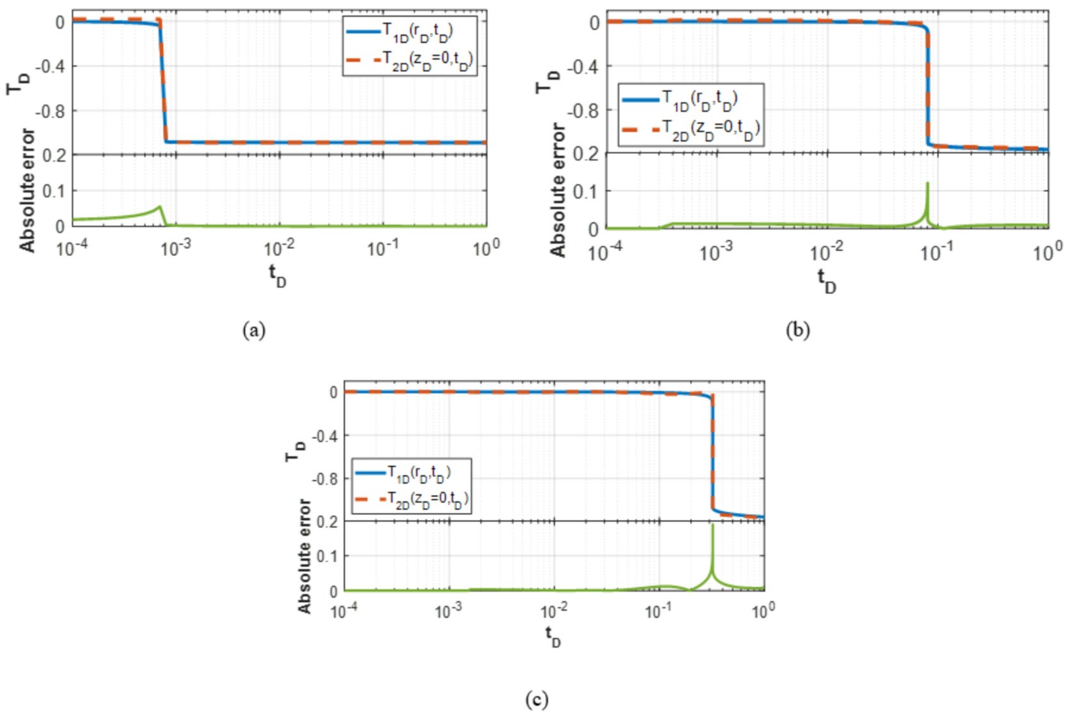

Figure 3. Temperature history at the distance for panel (a) $r_D = 0.002$ (b) $r_D = 0.02$ (c) $r_D = 0.04$.

In this study, we establish the criteria for validity by setting a 10% margin of disparity (absolute error of 0.1) between the temperature inside the reservoir and the temperature at the interface between the reservoir and the adjacent layer ($z_D = 0$ in Figure 1). From the plots in Figure 3, we observe a good agreement between the profiles for all temporal and spatial domains, except the temperature front. The error exceeds the 10% margin at the front in Figures 3b and 3c, as the temperature propagates further into the reservoir. The error at the front is lowest near the injection well (Figure 3a).

Figure 4 presents the impact of J-T number (A), heat-exchange number (B), and temperature front velocity (V) (see Equations 10–12) on $T_{1D}(z_D = 0, t_D)$ and $T_{2D}(r_D, t_D)$ histories at a fixed position of $r_\mathrm{D} = 0.002$. While parameter B has a negligible effect on the two profiles (Figure 4b), variations of A (Figure 4a) and V (Figure 4c) show significant effect on both profiles. As A approaches zero, the JT effect becomes less significant, leading to increased agreement between the reservoir and boundary histories. For large values of temperature front velocity V, the divergence between the profiles decreases.

Based on Figures 3 and 4, we observe that the deviation between the two profiles depends on the distance from injection well, the time of injection and the dimensionless group of constants A, B and V.

5. Analysis of the Solution

Figure 5 compares the temperature profiles at different times for the cases with unsteady-state (Equation 16) and steady-state heat exchange as derived by Chesnokov et al. (2024).Changing the sink-source term in a hyperbolic equation does not change the shock velocity; therefore, the positions of temperature fronts in both cases coincide and is given by the following equation:

$$x = x_w + 2Vt_D,\ x = r_D^2 \tag{18}$$

For times earlier than the stabilization time of the SS model (15 years), the NSS and the SS models show differences only behind the temperature front, while aligning ahead of it. At the stabilization time of the SS model, the temperature stops propagating into the reservoir, whereas the NSS model does not have a stabilized front,

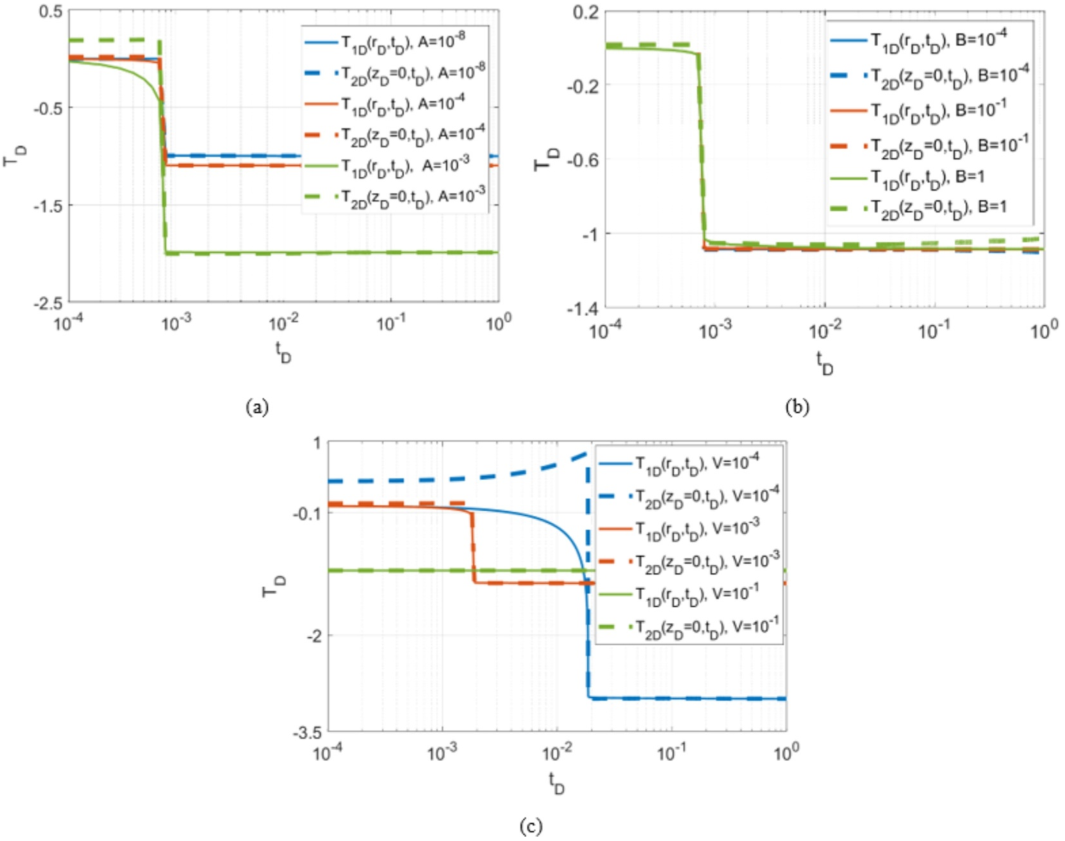

(a)

(b)

(c)

Figure 4. Effect of the dimensionless constants (a) JT number A (b) Heat exchange number B (c) Temperature front velocity V on the history of the reservoir and boundary temperatures, $T_{2D}(r_D,t_D)$ and $T_{1D}(z_D = 0,t_D)$, at $r_D = 0.002$.

resulting in lower temperatures. The position of the CO_2 front, where $T = T_I$, is presented in the second subplot indicating the domain 0 in Figure 2.

The pressure drop from well to reservoir is shown in the third subplot. Here we assume constant gas viscosity, so pressure drop is calculated directly from Darcy's law given by Equation 4. Since the pressure distribution is proportional to the logarithm of r, plotting the pressure drop (p-p_w) versus the radial distance in semi-log co-ordinates results in a straight line in Figure 5.

The injected gas displaces water with temperature T_I. The gas expands into the domain with lower pressure and cools down due to expansion. Simultaneously, it is heated by the rock containing connate water, where the gas flows. The assumption of the same temperature of the rock, connate water, and gas yields instant heat exchange between those three components.

Non-steady state heating of the reservoir by the surrounding formations contributes less heat to the system than a steady-state model, thus causing a lower temperature behind the cold front (zone II). The two heat exchange models show a positive gradient ahead of the temperature front (zone I) until the steady-state heat model stabilizes (as indicated by the green dashed curve at 15 years) and the front disappears. In the rear part of zone I, which expands from the well, the temperature gradient is negative. This negative gradient is due to the quasi steady-state flow near the well and the positive JT coefficient for CO_2. In each point r_D, the temperature decreases over time, indicating that the JT effect dominates over the heating of the reservoir by the surrounding layers. The slope of the profile trajectories in zone II for both models is equal to the JT coefficient of CO_2 at injection well. As the distance from the well increases, the slope deviates from the value of the JT coefficient at the minimum temperature.

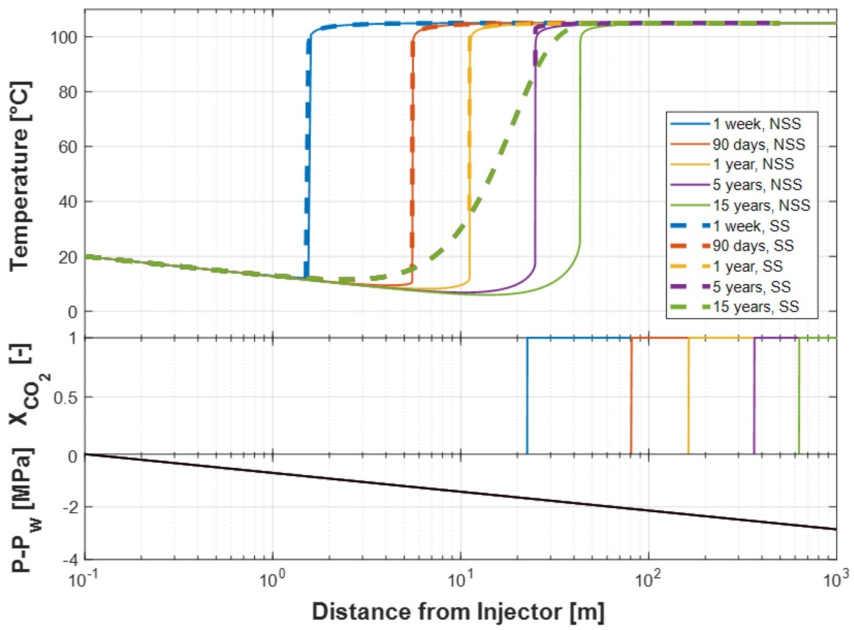

Figure 5. The impact of the NSS heat exchange on the temperature profiles (solid lines) in comparison to the SS heat exchange (dashed lines) from Chesnokov et al. (2024), CO_2 front position and pressure drop for varying times.

6. Risk Assessment for Hydrate Formation

The model developed in this paper can be utilized as a fast tool to screen depleted gas reservoirs for CO_2 storage, estimate expected CO_2 temperatures, and to assess the risk of hydrate formation. Moreover, the analytical model (Equation 16) allows determining the injection parameters (e.g., maximum injection rate) to avoid cold temperatures and/or hydrate formation, which is important for maintaining CO_2 injectivity. Among the design parameters, injection rate and product of permeability and the reservoir thickness ($k \times h$) highly affect the JT number A in Equation 10. Another critical system parameter affecting the likelihood of hydrate formation is the injection temperature T_J. As Aghajanloo et al. (2024) highlight, injecting CO_2 at a temperature lower than the hydrate equilibrium temperature (T_{hyd}) leads to hydrate creation near the wellbore, while CO_2 injected at a temperature higher than T_{hyd} results in a (possible) dry-out zone near injection well and a hydrate zone at a distance.

Figure 6a shows a CO_2-water phase diagram, displaying temperatures and pressures corresponding to the conditions in depleted gas fields and injection wells (Voronov et al., 2016). At high pressures, where compressibility

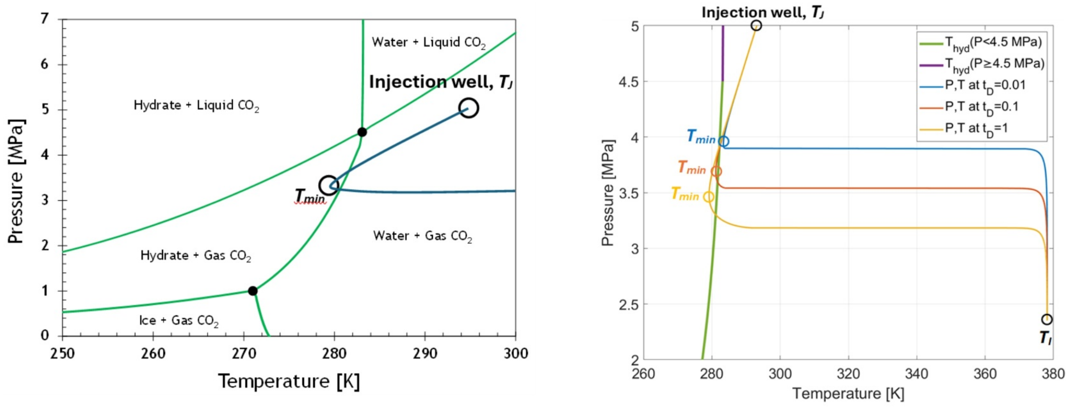

(a) (b)

Figure 6. (a) CO_2-water phase diagram reproduced from Voronov et al. (2016), with a T-P plot corresponding to $t_D = 1$ (b) T-P plots diagram for $t_D = 0.01, 0.1, 1$.

of gas can be neglected, the phase envelope for hydrates is almost vertical, that is, the hydrates appearance is determined mainly by hydrate formation temperature while at low pressures, the hydrates envelope is curvilinear. Yamada et al. (2024) fitted the hydrate curve (hydrate formation temperature) as a quadratic equation for $P < 4.5$ [MPa] and as a straight line for $P \geq 4.5$ [MPa]. We can use Equation 15 to find the minimum temperature with respect to r_D for different times. Since the minimum occurs behind the temperature front (Figure 5), we use the expression in Equation 15 for the temperature profile in domain II:

$$\begin{aligned}\frac{\partial T_D(r_D,t_D)}{\partial r_D} &= -\frac{2Br_D}{2V-1}e^{\frac{2B}{2V-1}\left(\sqrt{t_D-(r_D{}^2-r_{Dw}{}^2)}-\sqrt{t_D-\frac{r_D^2-r_{Dw}^2}{2V}}\right)}\\ &\left[\frac{1}{2V\sqrt{t_D-\frac{r_D^2-r_{Dw}^2}{2V}}}-\frac{1}{\sqrt{t_D-\left(r_D^2-r_{Dw}^2\right)}}\right]\\ &+\frac{2ABr_D}{V(2V-1)\sqrt{t_D-\left(r_D^2-r_{Dw}^2\right)}}e^{\frac{2B}{2V-1}\sqrt{t_D-\left(r_D^2-r_{Dw}{}^2\right)}}\\ &\int_{r_{Dw}}^{r_D}\frac{1}{k}e^{-\frac{2B}{2V-1}\sqrt{t_D-\left(k^2-r_{Dw}^2\right)}}dk-\frac{A}{Vr_D},\ t_D > \frac{r_D^2-r_{Dw}^2}{2V}\end{aligned} \tag{19}$$

Equating the temperature gradient in Equation 19 to zero yields the transcendent equation with respect to either r_D or t_D, defining the trajectory of the minimum temperature point:

$$r_{D\min} = r_{D\min}(t_D), \quad t_{D\min} = t_{D\min}(r_D) \tag{20}$$

For example, $t_D = 1$ corresponds to $r_{D\min} = 0.026$.

The trajectory of the minimum temperature point as parametrized by r_D in the phase diagram (blue curve in Figure 6a), is given by:

$$T_D = T_{D\min}(r_{D\min}) = T_D(r_{D\min}, t_D(r_{D\min})),\ p_D = p_D(r_{D\min}) \tag{21}$$

The temperature where hydrates begin to form for high pressures is defined by the point where the trajectory in Equation 21 meets the function T_{hyd} $(P \geq 4.5)$ (Yamada et al., 2024):

$$T_{\text{hyd}} = 0.1714P + 282.39 \tag{22}$$

For low pressures, the hydrate formation temperature is defined by the temperature trajectory meeting T_{hyd} $(P < 4.5)$ (Yamada et al., 2024):

$$T_{\text{hyd}} = 0.1696P^3 - 2.1877P^2 + 10.952P + 262.69 \tag{23}$$

Figure 6b presents profiles of temperature $T(r,t)$ and pressure $P(r,t)$ at three fixed moments, where the expressions of $T(r,t)$ and $P(r,t)$ are given by Equations 4 and 16, respectively. The parameter along the three curves is radius; each curve starts at wellbore radius ($r = r_w$) and extends to the outer boundary (r_e) given by Equation 5. For the moment $t_D = 0.01$, $T_{\min} > T_{\text{hyd}}$ at the point $r_{\min}$, meaning that no hydrates have been formed during this time. The curve that corresponds to $t_D = 0.1$ crosses the phase envelope ($T_{\min} < T_{\text{hyd}}$); the radii of the entrance and exit points for the hydrate domain of the phase diagram correspond to the distances where the hydrates are formed. At $t_D = 1$, the hydrate formation zone is widest (third curve). A more accurate determination of the T-P trajectory inside the hydrate zone can be obtained by solving the non-isothermal, multicomponent flow equations at the presence of a solid hydrate phase (Aghajanloo et al., 2024). The derived model effectively predicts the position of the T-P trajectory in the absence of hydrates and indicates whether hydrates are likely to form.

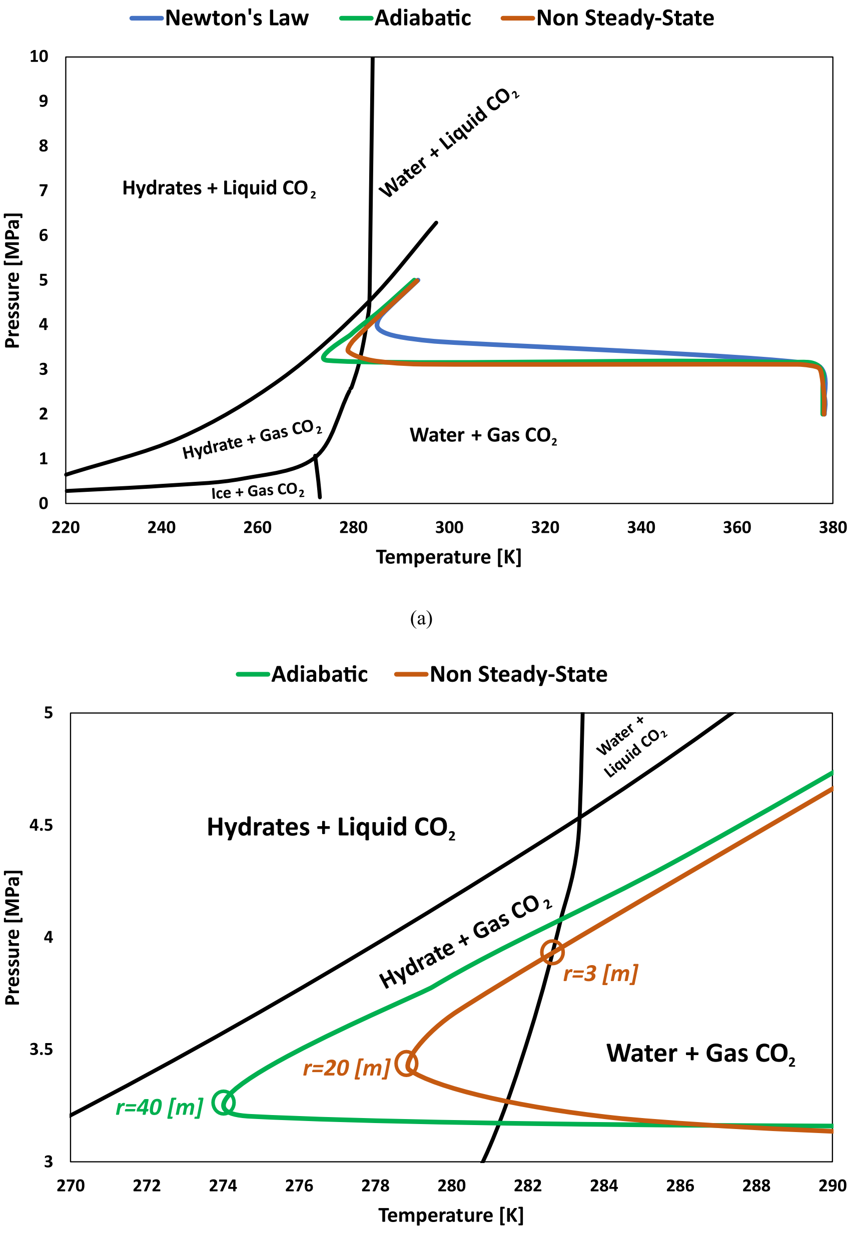

Figure 7. (a) T-P trajectories for different heat exchange models on a binary CO_2-water phase diagram at the moment $t_D = 1.5$. (b) Adiabatic and NSS curves in the Hydrate + Gas CO_2 zone.

Figure 7 shows the projection of the *T-P* curve onto the phase diagram for the heat exchange models -adiabatic (no heat transfer from adjacent layers to the reservoir), steady-state (Newton's law of heat transfer), and non-steady-state (vertical transient heat wave)—from well to reservoir conditions. Subsequently, we calculate the position of the minimum temperature point within the reservoir for each model. This analysis determines the potential risk of hydrate formation near the injection well, which could lead to injectivity impairment. All the models were subjected to similar reservoir and fluid characteristics, time of injection and other flow parameters.

Both the adiabatic and non-steady-state (NSS) heat exchange models demonstrate trajectories that extend into the hydrate formation zone. In contrast, the steady-state (SS) model remains outside the hydrate region, due to

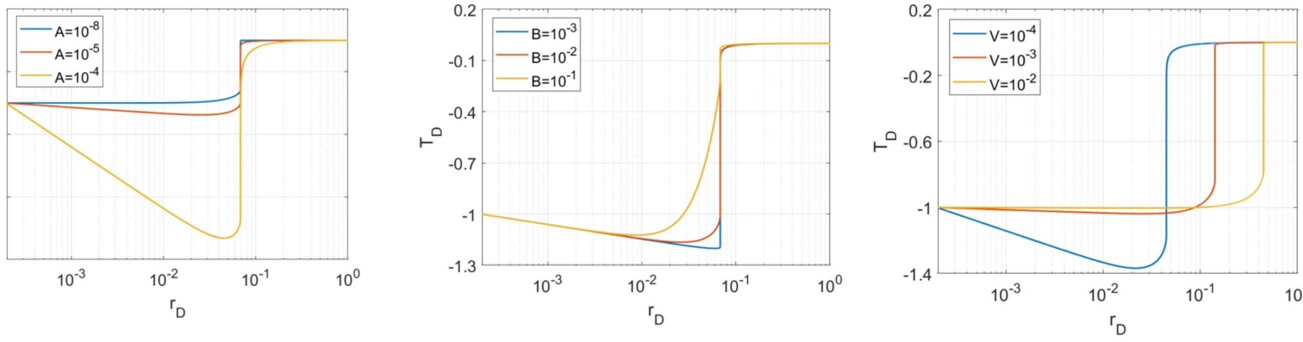

(a) (b) (c)

Figure 8. Effect of dimensionless parameters of the temperature profile at $t_D = 1$ (a) JT number A. (b) Heat exchange number B. (c) Temperature front velocity V.

excessive heat supplied by the surrounding formations. The adiabatic model exhibits the deepest penetration into the reservoir, while the non-steady-state model penetrates slightly shallower. Notably, based on the parameters in Table 1 (base case), the non-steady state model experiences its minimum pressure and temperature at a location far from the injection well ($r_{\min} = 20$ [m]), and crosses the hydrate phase curve at $r = 3$[m]. This suggests that any hydrates formed are unlikely to affect well injectivity.

7. Sensitivity Analysis

This section investigates the sensitivity of the temperature profiles to the constants A, B and V, presented in Equations 10–12. Substitution of the temperature front velocity V (Equation 12) into JT number A (Equation 10) yields the following form of constant A:

$$A = \frac{\alpha_{JT} V}{(T_I - T_J)} \frac{\mu q}{2\pi h K_{\text{rgwi}} k} \tag{24}$$

Integration of Darcy's law (Equation 4) from injection well r_w to position of CO_2 front at injection time, r_e, gives:

$$\frac{\mu q}{2\pi h K_{\text{rgwi}} k} = \frac{p_w - p_e}{\ln\left(\frac{r_e}{r_w}\right)} \tag{25}$$

here p_e ($\mathrm{ML^{-1}T^{-2}}$) is the pressure at r_e. Substituting the solution in Equation 25 into JT number A in Equation 24 gives:

$$A = \alpha_{\text{JT}} V \left[\ln\left(\frac{r_e}{r_w}\right)\right]^{-1} \frac{\Delta p}{\Delta T}, \ \Delta T = T_I - T_J, \ \Delta p = p_w - p_e \tag{26}$$

Equation 26 shows that the JT number A is the ratio between JT-induced temperature variation and the temperature gradient in the reservoir. An increase in A corresponds to an increase in the cooling effect. The increase in the heat exchange number B (Equation 10) reflects increase in the heat supplied by the surroundings to the reservoir. Increase in the temperature front velocity V corresponds to the increase in the heat capacity of the displacing fluid and decrease in the rock and water heat capacities.

Figure 8 illustrates the sensitivity of the temperature profile to the constants A, B, and V at $t_D = 1$. The effect of each parameter is examined using the values provided in Table 1, while keeping all other parameters constant. Figure 8a shows that high value of A results in a large temperature drop. This is attributed to a larger JT effect, which induces cooling in the system. Following Equation 26, the large cooling effect is caused by combined effects of a higher value of the JT coefficient, a larger value of the pressure drop, as well as a higher value of the temperature front velocity, V.

Figure 8b demonstrates the impact of the heat exchange number B on the temperature profile. Higher values of B correspond to increased heat supplied by the surrounding formations, which leads to higher temperatures in the system. From Equation 10, increase of the heat supplied by the surroundings is predominantly caused by larger heat conductivity of the adjacent formations and smaller reservoir thickness. As the value of B increases, the temperature profile tends to a steady-state form (Chesnokov et al., 2024).

In Figure 8c the variation in temperature front velocity V significantly affects both the minimum temperature and the position of the temperature front. According to Equation 12 V is the ratio between the thermal properties of the gas and the thermal properties of the reservoir (gas, water and solid). Higher values of V result in the temperature front propagating deeper into the reservoir and a smaller drop in the temperature. This indicates that an increase in the gas density and thermal capacity leads to faster temperature propagation.

In Equations 4, 24, and 25 the injected gas viscosity is constant (see assumption (h) in Section 2.1). So, the temperature field does not affect the reservoir pressure. It allows applying the analytical model (Equation 16) for temperature calculations in heterogeneous reservoirs with isolated layers. The heat waves from different layers interact in the adjacent impermeable layers, so the analytical model is valid for the injection durations lower than the times of vertical temperature propagation between the permeable layers, that is, $t < l^2/a$, where l is the distance between the neighboring layers and a is the thermal diffusivity of the adjacent formations.

Another extension for the analytical model (Equation 16) corresponds to a two-phase non-isothermal transport in porous media, including a two-phase flow model of CO_2 injection into aquifers. Equation 2 can be obtained by splitting from Buckley-Leverett equation that expresses mass balance of a two-phase incompressible fluid (Borazjani & Bedrikovetsky, 2017). Lifting solution (Equation 16) from the auxiliary space to the space of independent variables "temperature-saturation" of the governing system yields the exact solution for two-phase non-isothermal CO_2 injection.

8. Conclusions

This paper presents an analytical model of radial CO_2 injection into a low-pressure porous field accounting for Joule-Thomson cooling under unsteady heat exchange. While the previous work by Chesnokov et al. (2024) focused on analytical model with Joule-Thomson effect and the steady-state Newton's heat exchange that corresponds to thin impermeable shales surrounding the reservoir, this study extends the model to a unsteady state heat exchange. The geological setting of direct contact between the reservoir and the adjacent layers, which correspond to unsteady-state heat exchange, is more realistic than that of two thin shales at the top and the bottom of the reservoir, that separates the reservoir from overburden and under-burden formations where the temperature is maintained at the initial level T_I. This new model provides an analytical solution for geological structures where the reservoir is in direct contact with semi-infinite adjacent layers, rather than being surrounded by thin impermeable shales. The solution obtained in this model exhibits three temperature domains separated by gas and temperature fronts. The validity of the analytical model is determined by coupling of reservoir profile $T(r,t)$ with a quasi 2D (r,z) heat conductivity solution, using the same heat exchange term at the interface, $z = 0$. The deviation between the two solutions marginally exceeds 10% of the difference between the injected and initial temperatures only in the thin neighborhood of the temperature front.

For high-pressure injection of supercritical gas, where the hydrate envelope is almost independent of pressure and is given by hydrate temperature $T = T_{\mathrm{hyd}}$, the maximum hydrate-free rate is determined by minimum temperature, $T(r,t_{\min}(r)) > T_{\mathrm{hyd}}$. For low-pressure injection of gaseous CO_2, where the curvilinear hydrate envelope depends on both pressure and temperature, the maximum rate at each time is given by the point of contact between the envelope and profile trajectories. The intersection of the profile trajectories with the hydrate envelope indicates the distance at which hydrate formation initiates. Comparing the unsteady-state heat exchange model with the steady-state and adiabatic models, we find that the steady-state model penetrates the least into the reservoir, the adiabatic model penetrates the deepest, and the unsteady-state model falls in between.

Appendix A: Heat Exchange Between the Reservoir and the Surrounding Layers

To obtain the approximate expression for the heat exchange rate between the reservoir and the adjacent layers and close the energy balance equation in 1D flow model (Equation 2), here we discuss 2D (x,z,t) heat transfer equation. The assumption of zero heat conductivity in lateral direction yields a 1D equation for heat transfer over vertical:

$$\frac{\partial T}{\partial t} = a\frac{\partial^2 T}{\partial z^2}; \tag{A1}$$

where a is the thermal diffusivity of the adjacent formations, defined as,

$$a = \frac{\gamma}{\phi\rho_w C_{p_w} + (1-\phi)\rho_s C_{p_s}} \tag{A2}$$

The initial condition for vertical layers corresponds to initial reservoir temperature:

$$T(z, t=0) = T_I \tag{A3}$$

At this stage, the temperature on the reservoir-formation interface is assumed to be constant, that is, the boundary condition is:

$$T(z=0, t) = T_J \tag{A4}$$

The boundary condition at infinity corresponds to reaching reservoir temperature throughout the formation at infinite time:

$$T(z\rightarrow\infty, t) = T_I \tag{A5}$$

The solution to Equation A1 is self-similar; it is given by the following expression (Polyanin & Nazaikinskii, 2016):

$$T(z,t) = f\left(\frac{z}{2\sqrt{at}}\right) = T_J - (T_r - T_I)\, erf\left(\frac{z}{2\sqrt{at}}\right) \tag{A6}$$

The heat flux on the interface is obtained by taking derivative of z at $z = 0$ in solution Equation A6:

$$Q = \gamma\left(\frac{\partial T}{\partial z}\right)_{z=0} = (T_I - T_r)\sqrt{\frac{\gamma\left[\phi\rho_w C_{p_w} + (1-\phi)\rho_s C_{p_s}\right]}{\pi t}} \tag{A7}$$

As we assume heat exchange is delayed until the arrival of the gas front, we introduce a delay in time in Equation A7 as:

$$\Delta = t - \frac{\pi r^2 - \pi {r_w}^2}{u} \tag{A8}$$

Substituting the time dependent $T(r,t)$ and Equation A8 into Equation A7 instead of T_r results in the reformulation of the heat exchange term as presented in Equation 1.

Appendix B: Energy Balance Derivation

Following the thermodynamical derivations for energy balance in porous medium by Lake (1989) and Onur and Çinar (2016), we derive the energy balance for single-phase radial transport. The energy conservation equation accounts for heat capacity of gas, water and solid, external energy advection of the gas phase, and the work done by gas against expansion:

$$r\frac{\partial}{\partial t}\left[\phi(1-S_{wi})\rho_g e_g+\phi S_{wi}\rho_w e_w+(1-\phi)\rho_s e_s\right]+\frac{\partial}{\partial r}\left(rv\left[\rho_g e_g+p\right]-k_T r\frac{\partial T}{\partial r}\right)=\frac{\gamma r}{h}\left(\frac{\partial T}{\partial z}\right)_{z=0} \tag{B1}$$

where e_g (ML^2T^{-2}), e_w (ML^2T^{-2}), and e_s (ML^2T^{-2}) are internal energies for gas, water, and solid, respectively, v (LT^{-1}) is gas velocity, and k_T ($MLT^{-3}K^{-1}$) is reservoir heat conductivity.

The energy flux term in left hand side (LHS) consists of advective and thermal-conductivity components, and the source term in right hand side (RHS) corresponds to heat exchange between the reservoir and the surrounding layers.

Gas volumetric injection rate is assumed constant:

$$q=2\pi rhv=-2\pi rh\frac{k}{\mu}\frac{\partial p}{\partial r} \tag{B2}$$

For a piston-like displacement of water by CO_2, behind the gas front, water is at connate saturation and gas is the only flowing fluid. Compressibility of water and solid are neglected, so the expressions of phase enthalpies are:

$$H_s=e_s;\ \ H_w=e_w;\ \ H_g=e_g+\frac{p}{\rho_g} \tag{B3}$$

where H_s (ML^2T^{-2}), H_w (ML^2T^{-2}), and H_g (ML^2T^{-2}) are enthalpies of solid, water, and gas, respectively. Substitution of Equations B2–B3 into Equation B1 gives:

$$r\frac{\partial}{\partial t}\left[\phi(1-S_{wi})\rho_f H_f+\phi S_{wi}\rho_w H_w+(1-\phi)\rho_s H_s\right]-r\phi\frac{\partial p}{\partial t}+\frac{\partial}{\partial r}\left(\frac{q}{2\pi h}\rho_f H_f-k_T r\frac{\partial T}{\partial r}\right)=\frac{\gamma r}{h}\left(\frac{\partial T}{\partial z}\right)_{z=0} \tag{B4}$$

The total variation of gas enthalpy, H (ML^2T^{-2}), is:

$$dH_g=\left(\frac{\partial H_g}{\partial T}\right)_p dT+\left(\frac{\partial H_g}{\partial P}\right)_T dp=C_p dT-\alpha_{JT}C_p dp \tag{B5}$$

Here the heat capacity at constant pressure, C_p ($L^2T^{-2}K^{-1}$), and the JT coefficient are expressed as:

$$C_p=\left(\frac{\partial H_g}{\partial T}\right)_p,\alpha_{JT}=-\left(\frac{\partial H}{\partial p}\right)_T\left(\frac{\partial H}{\partial T}\right)_p^{-1} \tag{B6}$$

Equation B5 contains enthalpy variation over temperature and pressure due to gas compressibility. For incompressible solid and water, the term dp is negligible, and the total derivative of solid, water, and gas enthalpies is:

$$dH_s=C_{p_s}dT \tag{B7}$$

$$dH_w=C_{p_w}dT \tag{B8}$$

$$dH_g=C_{p_g}dT-\alpha_{JT}C_{p_g}dp \tag{B9}$$

The assumption of a constant injection rate, Equation B2, and constant injection pressure implies steady state pressure distribution *p(r)*:

$$q=-2\pi rh\frac{k}{\mu}\frac{\partial p}{\partial r}=const.\rightarrow\frac{\partial p}{\partial t}=0 \tag{B10}$$

Therefore, substitution of Equations B7–B10 into Equation B4 gives,

$$r\left[(1-\phi)\rho_s C_{p_s} + \phi(1-S_{wi})\rho_g C_{p_g} + \phi S_{wi}\rho_w C_{p_w}\right]\frac{\partial T}{\partial t} + \frac{\partial}{\partial r}\left(\frac{q}{2\pi h}\rho_g C_{p_g}\left[T-\alpha_{JT}p\right] - k_T r\frac{\partial T}{\partial r}\right) = \frac{\gamma r}{h}\left(\frac{\partial T}{\partial z}\right)_{z=0} \quad \text{(B11)}$$

Introducing dimensionless parameters (Equation 8) into energy-conservation Equation B11 yields dimensionless group in front of the last term in LHS, containing the injection period t_j in denominator. Therefore, for large-time approximation, where this dimensionless group tends to zero, heat conductivity in direction r is neglected. Substituting the heat exchange term from Equation 1 into Equation B11 and neglecting the conductive heat flux yields the energy balance in Equation 2.

Appendix C: Analytical Solution

Introducing the following change of variable in Equation 9:

$$x = {r_D}^2;\; x_w = {r_{Dw}}^2 \quad \text{(C1)}$$

Substituting the linear variable from Equation C1 into Equations 9–14, we obtain the following linear initial-boundary value problem for PDE:

$$\frac{\partial T_D}{\partial t_D} + 2V\frac{\partial T_D}{\partial x} = -\frac{A}{x} - B\frac{T_D}{\sqrt{t_D-(x-x_w)}}; \quad \text{(C2)}$$

$$T_D(x = x_w, t_D) = -1 \quad \text{(C3)}$$

$$T_D(x = x_w + t_D, t_D) = 0 \quad \text{(C4)}$$

The system presented in Equations C2–C4 is solved by the method of characteristics (Polyanin & Zaitsev, 2003).

Equation C2 in characteristic form is:

$$\frac{dt_D}{dx} = \frac{1}{2V} \quad \text{(C5)}$$

$$\frac{dT_D}{dx} + \frac{B}{2V}\frac{T_D}{\sqrt{t_D-(x-x_w)}} = -\frac{A}{2Vx} \quad \text{(C6)}$$

As it follows from Equation C5, the characteristic curves of Equation C2 are straight lines:

$$t_D = \frac{x-x_w}{2V} + c_1 \quad \text{(C7)}$$

where c_1 is a constant of integration, determined from the intersection point of characteristic line with the lines, where the initial and boundary conditions are posed. In zones I and II, Equation C7 takes the form-

$$t_{D2} = \frac{x_2-x_1}{2V} + t_{D1} \quad \text{(C7a)}$$

$$t_{D4} = \frac{x_4-x_w}{2V} + t_{D3}, \quad \text{(C7b)}$$

respectively.

Solving ordinary differential equation (ODE) in Equation C6 by the method of integrating factor, we obtain a general form of temperature profile for domains I and II as:

$$T_D = e^{\frac{2B}{2V-1}\sqrt{t_D-(x-x_w)}}\left(c_2 - \frac{A}{2V}\int_{x^*}^{x}\frac{1}{k}e^{-\frac{2B}{2V-1}\sqrt{t_D-(k-x_w)}}\,dk\right) \tag{C8}$$

where x^* is the starting position of propagation for characteristics and c_2 is constant of integration, determined from boundary conditions for each domain.

Solution in domain II: For the domain behind the temperature front, $t_D > \frac{x-x_w}{2V}$, the characteristic lines propagate from injection well. By substituting the boundary condition in Equation C3 into Equation C8, we determine the constant of integration c_2 in this region as:

$$c_2 = -e^{-\frac{2B}{2V-1}\sqrt{t_D-\frac{x-x_w}{2V}}} \tag{C9}$$

Substituting Equation C9 into the general form in Equation C8 and setting $x^* = x_w$ at the lower integral limit, we obtain the temperature profile for the domain behind the temperature front:

$$T_D(x,t_D) = e^{\frac{2B}{2V-1}\sqrt{t_D-(x-x_w)}}\left(-e^{-\frac{2B}{2V-1}\sqrt{t_D-\frac{x-x_w}{2V}}} - \frac{A}{2V}\int_{x_w}^{x}\frac{1}{k}e^{-\frac{2B}{2V-1}\sqrt{t_D-(k-x_w)}}\,dk\right) \tag{C10}$$

Solution in domain I: For the domain between the temperature front and the CO_2 front, $x - x_w < t_D < \frac{x-x_w}{2V}$, the characteristic lines propagate from the moving CO_2 front. By substituting the boundary condition in Equation C4 into Equation C8 we obtain the constant of integration c_2 in this region as:

$$c_2 = 0 \tag{C11}$$

Characteristics in this domain emanate from the CO_2 front, and their originating position is defined by the following function:

$$x^* = \frac{t_D + x_w - \frac{x}{2V}}{1 - \frac{1}{2V}} \tag{C12}$$

Further, substituting Equation C11 and the lower integral limit presented in Equation C12 into the general form Equation C8, we obtain the temperature profile for the domain ahead of the temperature front and behind the CO_2 front as:

$$T_D(x,t_D) = -\frac{A}{2V}e^{\frac{2B}{2V-1}\sqrt{t_D-(x-x_w)}}\int_{\frac{t_D+x_w-\frac{x}{2V}}{1-\frac{1}{2V}}}^{x}\frac{1}{k}e^{-\frac{2B}{2V-1}\sqrt{t_D-(k-x_w)}}dk \tag{C13}$$

Solution in domain 0: For the unperturbed domain ahead of the CO_2 front, $x - x_w > t_D$, the reservoir temperature is at initial state, that is;

$$T_D(x,t_D) = 0 \tag{C14}$$

Finally, combining the solutions derived for each domain, as presented in Equations C10, C13, C14, we obtain the overall reservoir temperature profile in linear coordinates as:

$$T_D(x,t_D) = \begin{cases} e^{\frac{2B}{2V-1}\sqrt{t_D-(x-x_w)}}\left(-e^{-\frac{2B}{2V-1}\sqrt{t_D-\frac{x-x_w}{2V}}} - \dfrac{A}{2V}\displaystyle\int_{x_w}^{x}\frac{1}{k}e^{-\frac{2B}{2V-1}\sqrt{t_D-(k-x_w)}}\,dk\right), & t_D > \dfrac{x-x_w}{2V} \\ -\dfrac{A}{2V}e^{\frac{2B}{2V-1}\sqrt{t_D-(x-x_w)}}\displaystyle\int_{\frac{t_D+x_w-\frac{x}{2V}}{1-\frac{1}{2V}}}^{x}\frac{1}{k}e^{-\frac{2B}{2V-1}\sqrt{t_D-(k-x_w)}}\,dk, & x-x_w < t_D < \dfrac{x-x_w}{2V} \\ 0, & x-x_w > t_D \end{cases} \tag{C15}$$

Expressing x versus r_D from Equation C1 and substituting it into Equation C15, we obtain the dimensionless radial solution, Equation 15. Subsequently, substitution of the dimensionless variables in Equations 8, 10–12 into Equation 15, gives the dimensional solution in Equation 16.

Appendix D: The Validity Domain for Heat Exchange Model

In this section, we discuss the validation of the non-steady state heat exchange model used in our work, as presented in Equation 1. The approach involves the comparison of the temperature profile inside the reservoir (Equation 15) with the temperature profile on the interface between the reservoir and the adjacent formations.

At a constant radial distance from injection point, Equation 1 for heat exchange becomes a function of time only, given by the following form:

$$Q(t) = -\sqrt{\frac{\gamma\left[\phi\rho_w C_{p_w} + (1-\phi)\rho_s C_{p_s}\right]}{\pi}}\,\frac{(T(t)-T_I)}{\sqrt{t-\frac{\pi r^2-\pi {r_w}^2}{u}}} \tag{D1}$$

Vertical heat conductivity in the adjacent formations is given as:

$$\frac{\partial T}{\partial t} = a\frac{\partial^2 T}{\partial z^2} \tag{D2}$$

The initial condition for the vertical layers corresponds to initial reservoir temperature:

$$T(z,t=0) = T_I \tag{D3}$$

At the reservoir-formation interface, we impose a Neumann condition, which corresponds to the heat flux on the boundary $z = 0$:

$$\gamma\frac{dT}{dz}(z=0,t) = Q(t) \tag{D4}$$

Introducing the following dimensionless variables into Equations D2–D4:

$$T_D = \frac{T-T_I}{T_I-T_J};\ t_D = \frac{t}{t_j}; z_D = \frac{z}{\sqrt{at_j}}; \tag{D5}$$

We obtain the dimensionless form of equations for vertical heat conductivity:

$$\frac{\partial T_D}{\partial t_D} = \frac{\partial^2 T_D}{\partial {z_D}^2} \tag{D6}$$

$$T_D(z_D, t_D = 0) = 0 \tag{D7}$$

$$\frac{dT_D(z_D=0,t_D)}{dz_D}=\begin{cases}-\sqrt{\frac{1}{\pi}}\ \frac{e^{\frac{2B}{2V-1}\sqrt{t_D-(r_D{}^2-r_{Dw}{}^2)}}}{\sqrt{t_D-(r_D{}^2-r_{Dw}{}^2)}}\left(-e^{-\frac{2B}{2V-1}\sqrt{t_D-\frac{r_D{}^2-r_{Dw}{}^2}{2V}}}-\frac{A}{V}\int_{r_{Dw}}^{r_D}\frac{1}{k}e^{-\frac{2B}{2V-1}\sqrt{t_D-(k^2-r_{Dw}{}^2)}}\,dk\right), & t_D>\frac{r_D{}^2-r_{Dw}{}^2}{2V}\\ \frac{A}{V}\sqrt{\frac{1}{\pi}}\ \frac{e^{\frac{2B}{2V-1}\sqrt{t_D-(r_D{}^2-r_{Dw}{}^2)}}}{\sqrt{t_D-(r_D{}^2-r_{Dw}{}^2)}}\int_{\sqrt{\frac{\left(t_D+r_{Dw}{}^2-\frac{r_D{}^2}{2V}\right)}{1-\frac{1}{2V}}}}^{r_D}\frac{1}{k}e^{-\frac{2B}{2V-1}\sqrt{t_D-(k^2-r_{Dw}{}^2)}}\,dk, & r_D{}^2-r_{Dw}{}^2<t_D<\frac{r_D{}^2-r_{Dw}{}^2}{2V}\\ 0, & r_D{}^2-r_{Dw}{}^2>t_D\end{cases}\tag{D8}$$

Here, Neumann boundary condition in Equation D8 accounts for the dynamics of the heat flux imposed by the temperature change inside the reservoir, derived in Equation 15.

Based on the work of Polyanin and Nazaikinskii (2016), a general form of the solution to the problem presented in Equations D6–D8 is given:

$$T(z,t)=\frac{1}{2\sqrt{\pi a t}}\int_0^\infty\left\{e^{-\frac{(z-\xi)^2}{4at}}+e^{-\frac{(z+\xi)^2}{4at}}\right\}f(\xi)d\xi-\sqrt{\frac{a}{\pi}}\int_0^t\frac{e^{-\frac{z^2}{4a(t-\tau)}}}{\sqrt{t-\tau}}g(\tau)d\tau\tag{D9}$$

here *f(ξ)* represents the initial condition and *g(τ)* represents the flux imposed in the boundary. Substituting the variables in Equation D9 with the variables in Equations D6–D8, we arrive at the exact solution for vertical heat conduction:

$$T_D(z_D,t_D)=$$

$$\begin{cases}\left\{\frac{1}{\pi}\int_0^{t_D}\frac{e^{-\frac{z_D{}^2}{4(t_D-\tau)}}}{\sqrt{t_D-\tau}}\left[\frac{e^{\frac{2B}{2V-1}\sqrt{\tau-(r_D{}^2-r_{Dw}{}^2)}}}{\sqrt{\tau-(r_D{}^2-r_{Dw}{}^2)}}\left(-e^{-\frac{2B}{2V-1}\sqrt{\tau-\frac{r_D{}^2-r_{Dw}{}^2}{2V}}}-\frac{A}{V}\int_{r_{Dw}}^{r_D}\frac{1}{k}e^{-\frac{2B}{2V-1}\sqrt{\tau-(k^2-r_{Dw}{}^2)}}\,dk\right)\right]d\tau,\right. & t_D>\frac{r_D{}^2-r_{Dw}{}^2}{2V}\\ -\frac{A}{V\pi}\int_0^{t_D}\frac{e^{-\frac{z_D{}^2}{4(t_D-\tau)}}}{\sqrt{t_D-\tau}}\left[\frac{e^{\frac{2B}{2V-1}\sqrt{\tau-(r_D{}^2-r_{Dw}{}^2)}}}{\sqrt{\tau-(r_D{}^2-r_{Dw}{}^2)}}\int_{\sqrt{\frac{\left(\tau+r_{Dw}{}^2-\frac{r_D{}^2}{2V}\right)}{1-\frac{1}{2V}}}}^{r_D}\frac{1}{k}e^{-\frac{2B}{2V-1}\sqrt{\tau-(k^2-r_{Dw}{}^2)}}\,dk\right]d\tau, & r_D{}^2-r_{Dw}{}^2<t_D<\frac{r_D{}^2-r_{Dw}{}^2}{2V}\\ 0, & r_D{}^2-r_{Dw}{}^2>t_D\end{cases}\tag{D10}$$

To find the vertical temperature profile along the boundary between the reservoir and adjacent formation, we set z_D equals zero in Equation D10:

$$T_D(z_D = 0, t_D) = \begin{cases} \dfrac{1}{\pi}\displaystyle\int_0^{t_D} \dfrac{1}{\sqrt{t_D-\tau}}\left[\dfrac{e^{\frac{2B}{2V-1}\sqrt{\tau-(r_D{}^2-r_{Dw}{}^2)}}}{\sqrt{\tau-(r_D{}^2-r_{Dw}{}^2)}}\left(-e^{-\frac{2B}{2V-1}\sqrt{\tau-\frac{r_D{}^2-r_{Dw}{}^2}{2V}}}-\dfrac{A}{V}\displaystyle\int_{r_{Dw}}^{r_D}\dfrac{1}{k}e^{-\frac{2B}{2V-1}\sqrt{\tau-\left(k^2-r_{Dw}{}^2\right)}}\,dk\right)\right]d\tau, & t_D > \dfrac{r_D{}^2-r_{Dw}{}^2}{2V} \\[2ex] -\dfrac{A}{V\pi}\displaystyle\int_0^{t_D}\dfrac{1}{\sqrt{t_D-\tau}}\left[\dfrac{e^{\frac{2B}{2V-1}\sqrt{\tau-(r_D{}^2-r_{Dw}{}^2)}}}{\sqrt{\tau-(r_D{}^2-r_{Dw}{}^2)}}\displaystyle\int_{\sqrt{\frac{\left(\tau+r_{Dw}{}^2-\frac{r_D{}^2}{2V}\right)}{1-\frac{1}{2V}}}}^{r_D}\dfrac{1}{k}e^{-\frac{2B}{2V-1}\sqrt{\tau-\left(k^2-r_{Dw}{}^2\right)}}\,dk\right]d\tau, & r_D{}^2-r_{Dw}{}^2 < t_D < \dfrac{r_D{}^2-r_{Dw}{}^2}{2V} \\[2ex] 0, & r_D{}^2-r_{Dw}{}^2 > t_D \end{cases}$$

(D11)

The comparison of the temperature profile in the reservoir, Equation 15 and the temperature profile along the boundary, Equation D11 at fixed radial distances from injection well allows the determination of an area of validity for the heat exchange. The temperature profile along the interface for the vertical case is referred to as $T_{2D}(z_D = 0, t_D)$ and the temperature profile inside the reservoir is denoted as $T_{1D}(r_D, t_D)$.

Nomenclature

a	Thermal diffusivity of the adjacent formations [$\mathrm{m^2\ s^{-1}}$]
A	JT number [-]
b	Dimensional heat exchange number [$\mathrm{s^{-1/2}}$]
B	Heat exchange number [-]
C_p	Heat capacity [$\mathrm{J\ kg^{-1}\ K^{-1}}$]
C_{p_g}	Heat capacity of gas [$\mathrm{J\ kg^{-1}\ K^{-1}}$]
C_{p_s}	Heat capacity of solid [$\mathrm{J\ kg^{-1}\ K^{-1}}$]
C_{p_w}	Heat capacity of water [$\mathrm{J\ kg^{-1}\ K^{-1}}$]
e_g	Gas internal energy [J]
e_s	Solid internal energy [J]
e_w	Water internal energy [J]
h	Half of formation thickness [m]
H	Enthalpy [J]
H_g	Gas enthalpy [J]
H_s	Solid enthalpy [J]
H_w	Water enthalpy [J]
k	Permeability [$\mathrm{m^2}$]
k_T	Reservoir heat conductivity [$\mathrm{W\ m^{-1}\ K^{-1}}$]
K_{rgwi}	End-point relative permeability of CO_2 [-]
l	Distance between neighboring layers [m]
m	Dimensional JT number [$\mathrm{m^2\ s^{-1}}$]
p	Pressure [Pa]
p_w	Wellbore pressure [Pa]
p_D	Dimensionless pressure [-]
q	Half of injection rate [$\mathrm{m^3\ s^{-1}}$]
Q	Heat exchange [$\mathrm{W\ m^{-2}}$]
r	Radial variable [m]
r_w	Well radius [m]
r_e	Position of gas front at t_j [m]

r_f	Position of gas front [m]
r_D	Dimensionless radial variable [-]
r_{Dw}	Dimensionless well radius [-]
$r_{D\min}$	Dimensionless point of minimum temperature [-]
$r_{\min}$	Point of minimum temperature [m]
S_{wi}	Connate water saturation [-]
T	Temperature [K]
T_I	Initial temperature [K]
T_J	Injection temperature [K]
T_{hyd}	Hydrate formation temperature [-]
T_D	Dimensionless temperature [-]
$T_{D\min}$	Dimensionless minimum temperature [-]
$T_{\min}$	Minimum temperature [K]
T_{2D}	2D vertical temperature [-]
T_{1D}	1D reservoir temperature [-]
T_r	Temperature on the reservoir-formation interface [K]
t	Time [s]
t_j	Injection time [s]
t_D	Dimensionless time [-]
$t_{D\min}$	Dimensionless time corresponding to point of minimum temperature [-]
u	Effective injection rate per unit of the formation thickness [$\text{m}^2\ \text{s}^{-1}$]
v	Gas velocity on wellbore [m s^{-1}]
V	Temperature front velocity [-]
w	Dimensional temperature front velocity [$\text{m}^2\ \text{s}^{-1}$]
x	Dimensionless linear variable [-]
x^*	Dimensionless originating position for characteristics [-]
x_w	Dimensionless linear injection point [-]
z	Vertical variable [m]
z_D	Dimensionless vertical variable [-]

Greek characters

α_{JT}	Joule-Thomson coefficient [K Pa^{-1}]
γ	Adjacent formations heat conductivity [$\text{W m}^{-1}\ \text{K}^{-1}$]
Δ	Time of temperature front delay [s]
μ	Viscosity [Pa s]
ρ_g	Gas density [kg m^{-3}]
ρ_s	Solid density [kg m^{-3}]
ρ_w	Water density [kg m^{-3}]
ϕ	Porosity [-]

Abbreviations

JT	Joule–Thomson
LHS	Left hand side
NSS	Non-steady state
ODE	Ordinary differential equation

PDE	Partial differential equation
PVI	Pore volume injected
RHS	Right hand side
SS	Steady state
T-P	Temperature- Pressure

Conflict of Interest

The authors declare no conflicts of interest relevant to this study.

Data Availability Statement

Matlab R2022b software was used to simulate the analytical model, and all data are preserved at 10.5281/zenodo.14709427 and freely available through the Creative Commons Attribution License, open access (Chesnokov et al., 2025).

Acknowledgments

The authors thank Dr. Jeroen Snippe and Dr. Owain Tucker (Shell) for their valuable comments on the initial draft of the paper. The authors also thank Shell Global Solutions International for permission to publish this work. Open access publishing facilitated by The University of Adelaide, as part of the Wiley - The University of Adelaide agreement via the Council of Australian University Librarians.

References

Aghajanloo, M., Yan, L., Berg, S., Voskov, D., & Farajzadeh, R. (2024). Impact of CO2 hydrates on injectivity during CO2 storage in depleted gas fields: A literature review. *Gas Science and Engineering*, *123*, 205250. https://doi.org/10.1016/j.jgsce.2024.205250

Barrufet, M. A., Bacquet, A., & Falcone, G. (2010). Analysis of the storage capacity for CO2 sequestration of a depleted gas condensate reservoir and a saline aquifer. *Journal of Canadian Petroleum Technology*, *49*(8), 23–31. https://doi.org/10.2118/139771-PA

Bedrikovetsky, P. (1993). *Mathematical theory of oil & gas recovery*. Springer Science & Business Media. https://doi.org/10.1007/978-94-017-2205-6

Borazjani, S., & Bedrikovetsky, P. (2017). Exact solutions for two-phase colloidal-suspension transport in porous media. *Applied Mathematical Modelling*, *44*, 296–320. https://doi.org/10.1016/j.apm.2016.12.023

Chesnokov, C., Farajzadeh, R., Prempeh, K. O. K., Kahrobaei, S., Snippe, J., & Bedrikovetsky, P. (2024). Analytical model for Joule-Thomson cooling under heat exchange during CO2 storage. *Advances in Water Resources*, *190*, 104758. https://doi.org/10.1016/j.advwatres.2024.104758

Chesnokov, C., Prempeh, K. O. K., Farajzadeh, R., & Bedrikovetsky, P. (2025). Joule-Thomson cooling during CO2 injection under unsteady-state delayed heat exchange - Matlab Script [Computational Notebook]. *Zenodo*. https://doi.org/10.5281/zenodo.14709427

LaForce, T., Ennis-King, J., & Paterson, L. (2014). Semi-analytical solutions for nonisothermal fluid injection including heat loss from the reservoir: Part 1. Saturation and temperature. *Advances in Water Resources*, *73*, 227–241. https://doi.org/10.1016/j.advwatres.2014.08.008

Lake, L. W. (1989). *Enhanced oil recovery*. Prentice Hall.

Lawal, K. A. (2020). Applicability of heat-exchanger theory to estimate heat losses to surrounding formations in a thermal flood. *Journal of Petroleum Exploration and Production Technology*, *10*(4), 1565–1574. https://doi.org/10.1007/s13202-019-00792-5

Maloney, D. R., & Briceno, M. (2009). Experimental investigation of cooling effects resulting from injecting high pressure liquid or supercritical CO2 into a low pressure gas reservoir1. *Petrophysics-The SPWLA Journal of Formation Evaluation and Reservoir Description*, *50*(4).

Mathias, S. A., Gluyas, J. G., Oldenburg, C. M., & Tsang, C.-F. (2010). Analytical solution for Joule–Thomson cooling during CO2 geo-sequestration in depleted oil and gas reservoirs. *International Journal of Greenhouse Gas Control*, *4*(5), 806–810. https://doi.org/10.1016/j.ijggc.2010.05.008

Michael, K., Golab, A., Shulakova, V., Ennis-King, J., Allinson, G., Sharma, S., & Aiken, T. (2010). Geological storage of CO2 in saline aquifers—A review of the experience from existing storage operations. *International Journal of Greenhouse Gas Control*, *4*(4), 659–667. https://doi.org/10.1016/j.ijggc.2009.12.011

Moreno, Z., Anto-Darkwah, E., & Rabinovich, A. (2021). Semi-analytical modeling of rate-dependent relative permeability in heterogeneous formations. *Water Resources Research*, *57*(4), e2021WR029710. https://doi.org/10.1029/2021WR029710

Moreno, Z., & Rabinovich, A. (2021). Impact of sub-core-scale heterogeneity on meter-scale flow and brine displacement in drainage by CO2. *Water Resources Research*, *57*(1), e2020WR028332. https://doi.org/10.1029/2020WR028332

Norouzi, A. M., Niasar, V., Gluyas, J. G., & Babaei, M. (2022). Analytical solution for predicting salt precipitation during CO2 injection into saline aquifers in presence of capillary pressure. *Water Resources Research*, *58*(6), e2022WR032612. https://doi.org/10.1029/2022WR032612

Oldenburg, C. M. (2007). Joule-Thomson cooling due to CO2 injection into natural gas reservoirs. *Energy Conversion and Management*, *48*(6), 1808–1815. https://doi.org/10.1016/j.enconman.2007.01.010

Onur, M., & Çinar, M. (2016). Temperature transient analysis of slightly compressible, single-phase reservoirs. *SPE Europec featured at EAGE Conference and Exhibition*, 30. https://doi.org/10.2118/185586-MS

Pires, A. P., Bedrikovetsky, P. G., & Shapiro, A. A. (2006). A splitting technique for analytical modelling of two-phase multicomponent flow in porous media. *Journal of Petroleum Science and Engineering*, *51*(1), 54–67. https://doi.org/10.1016/j.petrol.2005.11.009

Polyanin, A., & Nazaikinskii, V. (2016). *Handbook of linear partial differential equations for engineers and scientists* (2nd ed.). Chapman and Hall/CRC. https://doi.org/10.1201/b19056

Polyanin, A., & Zaitsev, V. (2003). *Handbook of nonlinear partial differential equations*. Chapman & Hall/CRC Press. https://doi.org/10.1201/9780203489659

Rabinovich, A., Li, B., & Durlofsky, L. J. (2016). Analytical approximations for effective relative permeability in the capillary limit. *Water Resources Research*, *52*(10), 7645–7667. https://doi.org/10.1002/2016WR019234

Raimi, D., Zhu, Y., Newell, R. G., & Prest, B. C. (2024). Global energy outlook 2024: Peaks or plateaus.

Voronov, V. P., Gorodetskii, E. E., Podnek, V. E., & Grigoriev, B. A. (2016). Properties of equilibrium carbon dioxide hydrate in porous medium. *Chemical Physics*, *476*, 61–68. https://doi.org/10.1016/j.chemphys.2016.05.031

Yamada, K., Fernandes, B. R. B., Kalamkar, A., Jeon, J., Delshad, M., Farajzadeh, R., & Sepehrnoori, K. (2024). Development of a hydrate risk assessment tool based on machine learning for CO2 storage in depleted gas reservoirs. *Fuel (Guildford)*, *357*, 129670. https://doi.org/10.1016/j.fuel.2023.129670